PHYSICAL REVIEW B **85**, 035449 (2012)

Simulation of electromigration effects on voids in monocrystalline Ag films

A. Latz,[*] S. Sindermann, L. Brendel, G. Dumpich, F.-J. Meyer zu Heringdorf, and D. E. Wolf
Department of Physics and Center for Nanointegration Duisburg-Essen (CeNIDE), University of Duisburg-Essen, D-47057 Duisburg, Germany

(Received 6 September 2011; revised manuscript received 22 December 2011; published 30 January 2012)

We developed a three-dimensional, atomistic model based on the kinetic Monte Carlo method to investigate how voids penetrating a monocrystalline silver film are affected by electromigration. The simulations show a clear dependency between the nonequilibrium shape of the voids and the crystallographic orientation of the film. The simulation results are in accordance with experimental results on bicrystalline silver wires.

DOI: 10.1103/PhysRevB.85.035449 PACS number(s): 66.30.Qa, 81.07.Bc

I. INTRODUCTION

High current densities in integrated circuits can lead to the drift of metal ions and a concomitant failure of the circuit.[1,2] This effect is known as electromigration (EM). Reviews of the theory and electromigration induced effects can, for instance, be found in Refs. 3–5.

Phenomenologically there are two causes for the directed ion motion: the direct electrostatic force, exerted by the applied electric field on the ions, and the so-called wind force, which has its origin in the momentum transfer between the charge carriers and the ions.[3] Since both forces are proportional to the electric field $\vec{E}$, electromigration is commonly described by

$$\vec{F}_{\mathrm{EM}} = Z^* e\vec{E} = Z^* e\rho\vec{j}, \tag{1}$$

where Z^* denotes an effective valence of the metal ions, describing the combined effect of the direct and the wind force. e is the elementary charge, $\vec{j}$ is the current density, and ρ stands for the resistivity.

In the last two decades, there has been substantial effort to develop simulation models to investigate various EM-related phenomena. The relative long time and length scales (hours to days, respectively μm), on which electromigration effects take place, make an atomistic simulation, from a computational point of view, very difficult. Accordingly, numerous different models were introduced, e.g., based on continuous transport equations[6–10] or coarse grained models utilizing resistor networks,[11–13] which are able to bridge the length and time scales between EM phenomena and their underlying atomic processes. By neglecting atomic details, they could address several issues, e.g., the time to failure distribution, damage patterns, or resistance evolution of metallic lines. Even the motion and shape of a two-dimensional island under the influence of an electromigration force could be studied by Rusanen *et al.*[14] with a continuum model and validated by an atomistic kinetic Monte Carlo (kMC)[15–17] simulation. The simulation and the numerical solution of analogous three-dimensional models, however, would be many times more complex.

From an experimental point of view, it has recently become possible to investigate electromigration on the atomic scale,[18] and realistic three-dimensional atomistic models are needed. To save computational work, such models have so far been restricted to two dimensions,[14,19] with the exception of the work by Zaporozhets *et al.*[20] Their kMC model is able to simulate three-dimensional systems over reasonable time scales. This was achieved by utilizing a simple bond counting model to describe the interactions between nearest neighbors. For metals many-body potentials have been shown to be more suitable.[21,22] We developed a three-dimensional, atomistic model based on the kMC method, using a tight-binding potential.[22] The model has been calibrated along the lines proposed in Ref. 23 for silver (Ag). Our model is fast enough to simulate on one CPU comparatively large systems consisting of up to 10^5 atoms over time scales up to seconds, which is at least long enough to investigate electromigration phenomena under accelerated conditions, i.e., enhanced current density and temperature.

Our model allows us to investigate the influence of the crystallographic surface orientation of a monocrystalline Ag film[24,25] on electromigration induced voids. A characteristic nonequilibrium void shape dependent on the surface orientation is found and compared to experimental observations on bicrystalline Ag wires presented in this paper.

II. SIMULATION MODEL

The dynamical evolution of the investigated systems is described by thermally activated hopping processes of Ag atoms. In our model, atoms can only hop to unoccupied nearest-neighbor fcc sites, where the atom would have at least one occupied nearest neighbor. Exchange processes, where an atom exchanges with another atom, which continues the diffusive motion, are neglected, because their activation energies are either comparable or higher than those of the equivalent hopping processes.[26] The hopping rates are given by the Arrhenius law

$$\nu = \nu_0 \exp\left(-\frac{E_{\mathrm{a}}}{k_{\mathrm{B}}T}\right), \tag{2}$$

where ν_0 denotes the attempt frequency and E_{a} is the activation energy barrier, separating the initial and final configuration in the potential-energy surface (PES) of the system. k_{B} is the Boltzmann constant and T is the temperature. We assume a commonly used constant value[17] of $\nu_0 = 10^{12}\ \mathrm{s}^{-1}$.

Evolving the system in time requires the knowledge of every allowed process and its corresponding hopping rate. In each simulation step, one of these processes is chosen with a

©2012 American Physical Society

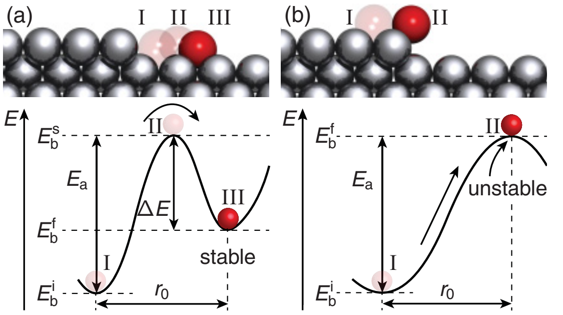

FIG. 1. (Color online) Schematic outline of the E_a composition for atom hops to stable (a) and unstable (b) fcc sites. (a) Binding energy curve for an atom detaching from a step. The saddle point is between the neighboring fcc sites. This is not the case in (b), which shows the binding-energy curve for an atom hopping over a step. There, the final fcc site is a saddle point.

probability proportional to its hopping rate. After performing the chosen process, the time is incremented by

$$\Delta t_{\mathrm{kMC}} = -\frac{1}{\nu_{\mathrm{total}}} \ln\left(\mathrm{Rnd}(0,1]\right), \tag{3}$$

where ν_{total} denotes the sum of all possible rates and Rnd(0,1] is a uniformly distributed random number between 0 and 1. The resultant accumulated time t_{kMC} corresponds to real time.[15] Before the next process can be chosen, the list of the allowed processes needs to be updated. To allow an efficient search and update of the rates, we use a binary tree to administrate them.[27,28]

To calculate the rate for an atom hop, one needs to know the corresponding activation energy E_a, which is the difference between the saddle-point energy E_b^s and the binding energy at the initial fcc site, E_b^i. The following parametrization turns out to be useful, because the saddle point lies between two fcc sites, the initial and the final one, which may be interchanged depending on the direction of the hop. Denoting the smaller activation energy of the two hop directions by ΔE, one can write

$$E_a = \Delta E + \max\left(E_b^f - E_b^i, 0\right). \tag{4}$$

Figure 1(a) illustrates this decomposition of E_a for an atom detaching from a step and hopping to a stable fcc site. The positions I, II, and III denote the minima (I, III) and the saddle point (II) on the PES along the hopping path.

Sites with less than three occupied nearest-neighbor sites ($Z = 1$, $Z = 2$) cannot represent a minimum in the PES. For $Z = 2$ they are (unstable) saddle points that need to be crossed to reach a neighboring stable site. Figure 1(b) shows E_a for an atom hopping over a step, during which an unstable fcc site must be taken as an intermediate position II. The activation energy E_a for a hop, which leads to such an unstable fcc site, is the difference of the binding energies at the "final" and initial site ($E_b^f - E_b^i$). There is no activation energy for the subsequent hop to a neighboring stable site. In the model we directly choose one of the possible stable nearest-neighbor sites with equal probability and do not increment t_{kMC} for the subsequent hop, i.e., the rate is regarded as infinite. Hence hops between unstable sites are excluded.

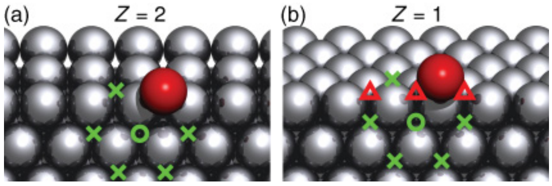

FIG. 2. (Color online) Vicinity of a fcc site (green circle) on a {100}/{111} edge (a) and a {111}/{111} edge (b), respectively (neighboring fcc sites are represented by green crosses). To reach an fcc site on the upper facet, an intermediate, unstable position (red atom) is taken on with $Z = 2$ (a) and $Z = 1$ (b). The latter is especially important, because due to the nonimplemented hcp sites (red triangles) traversing a {111}/{111} edge would be impossible otherwise.

Figure 2 shows the vicinity of a fcc site (green circle) on a {100}/{111} edge (a) and a {111}/{111} edge (b), respectively. Allowing hops to $Z = 2$ sites enables an atom to hop over an {100}/{111} edge. But in the latter case, the atom can still not cross the edge, as long as no hops to $Z = 1$ sites are allowed. In reality an atom would not traverse the $Z = 1$ sites, which represent maxima on the PES. Instead it would use a hcp site (red triangles) to reach the upper facet. In this sense, allowing hops to the $Z = 1$ sites represents a workaround for hcp sites of the lattice that are not implemented in the simulation. In accordance to this, the binding energies at the $Z = 1$ sites will be adjusted to those of the corresponding hcp sites.

The effect of the electromigration is implemented by lowering the activation energy for diffusion in the $\vec{F}_{\mathrm{EM}}$ direction and by raising it in the opposite direction. As a first approximation we used a constant electromigration force, thus the change of the activation energy is simply the work done by the EM force from the potential-energy minimum to the saddle point, which is assumed to lie in the middle of the diffusion path for stable hops:

$$\Delta E_{\mathrm{EM}} = -\vec{F}_{\mathrm{EM}} \frac{\vec{r}_0}{2}, \tag{5}$$

where $\vec{r}_0$ denotes the vector between the final and initial site. For hops to unstable fcc sites Eq. (5) is simply multiplied by 2, because now the distance between the initial site and the saddle point is the nearest-neighbor distance $|\vec{r}_0|$.

So, the complete activation energy is calculated by

$$E_a = \begin{cases} \max\left(E_b^f - E_b^i, 0\right) + \Delta E + \Delta E_{\mathrm{EM}} & Z > 2, \\ E_b^f - E_b^i + 2\Delta E_{\mathrm{EM}} & Z \leqslant 2. \end{cases} \tag{6}$$

III. SIMULATION PARAMETER AND SETUP

To describe the interactions between Ag atoms we use a many-body tight-binding-potential[22] and take interactions up to fifth-nearest neighbors into account. The contribution of the ith atom to the cohesive energy of the system ($E_c = \sum_i E_c^i$) consists of a binding many-body term and a repulsive pair term:

$$E_c^i = -\left(\sum_{j\neq i} \xi^2 \exp[-2q(r_{ij} - 1)]\right)^{1/2} + \sum_{j\neq i} A \exp[-p(r_{ij} - 1)]; \tag{7}$$

r_{ij} denotes the distance between the atoms i and j in units of r_0. The free parameters A, ξ, p, and q were fitted to experimental values of Ag by Cleri and Rosato.[22]

The binding energy of an atom i is defined as the difference between the cohesive energy of the system with and without the atom i:

$$E_{\mathrm{b}}^{i} = E_{\mathrm{c}} - E_{\mathrm{c}}(\vec{x}_i \to \infty). \tag{8}$$

Due to the binding many-body term, this calculation is computationally very expensive. In principle one has to completely recalculate the binding term with and without the atom i for all atoms in its interaction radius. To circumvent this, we performed minimal energy path (MEP) simulations[29] with the goal to find an approximation for E_{b}^{i}.

For the binding energies at the initial and final fcc site, our approximation for E_{b}^{i} consists of two parts: The direct contribution of the hopping atom E_{c}^{i}, which is calculated in a rigid fcc lattice with Eq. (7), and an empirical many-body correction E_{s}^{i}, which includes elastic effects and the contributions of the other atoms:

$$E_{\mathrm{b}}^{i} = E_{\mathrm{c}}^{i} + E_{\mathrm{s}}^{i}. \tag{9}$$

Due to the vast number of possible neighbor configurations within the interaction radius ($2^{78} \approx 3 \times 10^{23}$), one can only investigate some key configurations to find an ansatz for E_{s}^{i}. Experience shows that, e.g., adatom diffusion, edge diffusion, and vacancy diffusion are such key processes.[23] The initial and final configurations of these processes were used to find a model for E_{s}^{i}. In total we utilized 52 configurations,[30] including five $Z = 2$ configurations. We found by checking different approaches that for $Z > 2$, E_{s}^{i} can be well described by

$$E_{\mathrm{s}}^{i} = a \cdot Z^{i} + b \cdot \sqrt{Z^{i} \cdot \langle Z_{\mathrm{nn}}^{i} \rangle} + c, \tag{10}$$

where $\langle Z_{\mathrm{nn}}^{i} \rangle$ denotes the mean of Z of the occupied nearest neighbors of atom i. Equation (10) allows a huge speedup against the direct calculation of the binding energy, by utilizing easy to calculate variables. Using the 47 $Z > 2$ configurations, the fit parameters were determined by a least-squares fit as $a = -0.1424(\pm 0.0051)$ eV, $b = 0.1192(\pm 0.0007)$ eV, and $c = -0.6594(\pm 0.0229)$ eV.

Since typical activation energies are of the order 0.1 eV, the mean error of our approximation of about $0.0059(\pm 0.0052)$ eV is comparably small.

Our analysis showed that, due to strong elastic effects, Eq. (10) cannot describe $Z = 2$ configurations very well. E_{s}^{i} for the five analyzed $Z = 2$ configurations does not fluctuate strongly [$\langle E_{\mathrm{s},Z=2} \rangle = -0.425(\pm 0.023)$ eV], thus we use a fixed $E_{\mathrm{s},Z=2} = -0.425$ eV for every $Z = 2$ configuration. Because the fcc sites with $Z = 1$ represent, as described earlier, nonimplemented hcp sites with $Z = 2$, their activation energy is approximated by the average binding energy of the five analyzed $Z = 2$ configurations ($E_{\mathrm{b},Z=2} = -1.971$ eV).

To calculate the activation energy, a description for $E_{\mathrm{b}}^{\mathrm{s}}$, or equivalently ΔE, is still needed. To save computing time, we use a constant value ΔE for all processes in our model, instead of calculating it for every possible hopping process. Specifically, the mean value of 17 key elementary diffusion processes between differently configured stable initial and final sites is used: $\Delta E = 0.317(\pm 0.167)$ eV. Because the value for the vacancy diffusion (0.695 eV) deviates strongly from the mean value, we used for this important process the value derived by a minimal energy path simulation.

Under typical working conditions of an interconnect, electromigration phenomena take place on the time scale of several years. Hence accelerated conditions are used in experiments,[5,31,32] namely an increased current density and temperature. Typical current densities in EM experiments are of the order of 10^7 A/cm^2. For reasonable values of $Z^{*}e = -10e$ (Refs. 33 and 34) and $\rho_{\mathrm{Ag}} = 1.587 \times 10^{-8}\ \Omega\,\mathrm{m}$,[35] this results in an electromigration force of $F_{\mathrm{EM}} = 1.587 \times 10^{4}$ eV/m [cf. Eq. (1)]. This corresponds to a maximal change of the activation energy for a hop in the $\vec{F}_{\mathrm{EM}}$ direction of $\Delta E_{\mathrm{EM}} = -2.29 \times 10^{-6}$ eV [Eq. (5), $r_0 = 2.89$ Å (Ref. 35)]. Since characteristic activation energies are of the order 0.1 eV, a very long time would be required before EM induced effects occur. As in previous models,[14,19,20] we thus increase the current density and temperature even more. In detail we use an increased ΔE_{EM} value of 0.005 eV, that is still two orders of magnitude smaller than typical activation energies. The simulated temperature (800 K) is two times larger than in the experiments below (approximately 400 K). This is justified, because the frequencies of rare and frequent events differ still by several orders of magnitude. Therefore equilibrium between states connected by small energy barriers is still reached long before any of the slow events occurs, which are responsible for the long time evolution of the system.

Figure 3 shows the used simulation setup, consisting of a three-dimensional film of Ag atoms, which represents a section of a monocrystalline nanowire. In electromigration experiments one often observes voids, which penetrate the test structure and possibly lead to a failure of it. To investigate the characteristics of such voids in monocrystalline Ag we cut an initially cylindrical void with radius $15r_0$ into a film of $120 \times 120 \times 16$ atoms. The system size is chosen larger in the $\vec{z}$ direction to allow atoms to pile up. The occurring free top surface of the film is either the (111) or (001) surface of the fcc lattice and the electromigration force points in the $[\bar{1}\bar{1}2]$ or [110] direction.

Since it is not possible to simulate a complete μm-sized nanowire with contacts, reasonable assumptions for the boundary conditions are needed. In our model we use periodic boundary conditions (PBCs). In this sense, a void in the system is exposed to its self-induced vacancy flux. In contrast to open

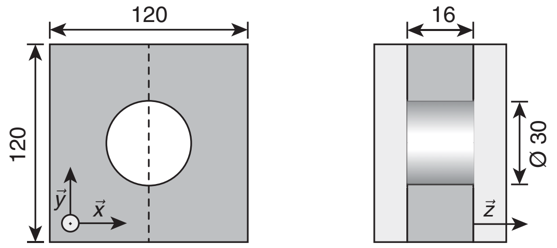

FIG. 3. The simulation setup: An initially cylindrical void is cut into a Ag stripe of $120 \times 120 \times 16$ atoms. $\vec{x}$ points in the $[11\bar{2}]$ or [110] direction, $\vec{y}$ points in the $[1\bar{1}0]$ direction and $\vec{z}$ points in the [001] or [111] direction.

boundary conditions (OBCs), with and without the insertion of single atoms or vacancies at the boundary, the PBCs have the advantage that the mass in the system is preserved. We are therefore able to investigate voids over long enough time scales, avoiding them to become too big or vanish.

Periodic boundary conditions in all three directions, without a free top and bottom surface, would be reasonable to investigate voids in the inner part of the wire. But according to our simulation results, the free surface has a non-negligible influence on different void characteristics.

IV. SIMULATIONS AND RESULTS

A. (111)-oriented Ag film

Starting with a (111)-oriented Ag film and $\vec{F}_{\mathrm{EM}} = 0$ permits the void to relax into equilibrium. The initially round void shape (see Fig. 3) becomes hexagonal after approximately 10^7 kMC steps and does not change significantly within 3×10^9 kMC steps [Fig. 4(a)], confirming that this is a stable configuration. Starting with a different initial void form (prism with three-sided base or cuboid) leads to the same equilibrium form.

As one can see from Fig. 4(b), the initially nonfacetted void surface relaxes to its thermodynamic equilibrium shape (Wulff shape[36]), which is strongly facetted, consisting of alternating low index {111} and {100} facets. These facets are those with the lowest surface energy for Ag.[37]

Figure 4(b) shows the void in Fig. 4(a) from the side after cutting it, along the dotted line. It can be seen that the upper half of the void surface is of the opposite facet configuration as the lower half and thus the void shape cannot become triangular by a reduction of the six possible {100} facets and a concomitant growth of the {111} facets with the lowest surface energy.[37] Figures 4(c) and 4(f) schematically show the lateral facets of the void surface.

The *ABC* stacking sequence of a fcc crystal in the [111] direction reduces the symmetry in the [111] direction from the sixfold symmetry of a {111} surface to a threefold symmetry and is thus responsible for the alternating {111} and {10 0} facets along the void surface.

When an electromigration force ($\Delta E_{\mathrm{EM}} = 0.005$ eV) is applied, the system cannot relax into equilibrium. The surface atoms drift, due to the lowering of the activation energy barrier, in the force direction.

The initially round void shape becomes again after approximately 10^7 kMC steps hexagonal, but the electromigration leads over time to an ablation of the facets on the upwind void side, leaving a pointed void shape, with the tip pointing opposite to $\vec{F}_{\mathrm{EM}}$ after 3×10^9 kMC steps [Figs. 4(d) and 4(e)]. The adjacent facets become larger at the same time. A further change of the shape cannot be observed within 10^{10} kMC steps. Reversing the electromigration direction would lead to the same void shape rotated by 180°.

A drift of the void (apart from the drift during the shape change) can rarely be observed (one to two atom layers during 10^{10} kMC steps). This has several reasons. For the ablation of an atom layer, a vacancy nucleus must nucleate on the corresponding facet. But the void facets are no perfect sinks for vacancies, because they can be evacuated over the top or bottom surface and thus a needed high vacancy density can rarely be achieved so that the drift velocity becomes limited by the nucleation rate. In addition, the mass transport along the void surface is not the only effect that leads to a void drift. In total three effects contribute to the void drift: First, the mass transport along the void surface. Second, the mass transport from the downwind void side out of the system in the electromigration direction, and third, the mass transport from the system boundary against $\vec{F}_{\mathrm{EM}}$ to the upwind void side. The second and third effect are equivalent to a detachment, attachment drift mechanism proposed by Tao *et al.*[18] Due to the PBC, the values of the second and third contributions are the same. If no void drift can be observed, the first and second contributions have to be the same, too, and the void is thus in a state of dynamic equilibrium.

The simulated void shapes in a (111)-oriented Ag film are in agreement with experimental observations for voids in the Ag(111) part of a bicrystalline test structure. Figure 5 shows a scanning electron microscopy (SEM) image of ten bicrystalline Ag nanowires after electrical stressing. The test structure was fabricated by a combination of self-assembly of bicrystalline Ag islands on a Si(111) surface[24] and focused ion beam (FIB) milling.[25] At sample temperatures around 500 °C and growth rates of approximately one monolayer per minute, some of the self-assembled Ag islands consist of two different crystallographic orientations, specifically Ag(111), where the [111] direction is oriented normal to the surface and Ag(001), where the [001] direction is normal to the surface.[24,38,39] The Ag(001) part and the Ag(111) part share the $[\bar{1}10]$ direction, i.e., that for a 90° grain boundary with respect to current direction, the electromigration force points along the $[\bar{1}\bar{1}0]$ direction in the Ag(001) part and along the $[\bar{1}\bar{1}2]$ direction in the Ag(111) part. The bicrystalline islands can be structured to nanowires with a single grain boundary of arbitrary direction by eroding material with a focused ion beam.[25] A special silicon on insulator (SOI) substrate is used to minimize leakage current through the substrate, the resistivity of which is changed by Ga doping of the used FIB. The SOI samples consist of a 2-μm-thick (111)-oriented device layer, a 1-μm-thick insulating oxide layer, and a 500-μm-thick handle layer. Due to this special substrate, the nanowires can be structured by at least 3-μm-deep trenches disconnecting the Ag nanowire from the rest of the substrate and are visible as dark lines in Fig. 5. The wires have typically a length of 11 μm, a width of 1 μm, and a height of approximately 100 nm. The test structure shown in Fig. 5 has a grain boundary (indicated by an orange dashed line) comprising a 90° angle with the wire edges. The Ag(001) part of the wires is on the left side of the grain boundary and the Ag(111) part of the wires is on the right side of the grain boundary. Depending on the direction of the electromigration force, which is decided by the polarity of the applied voltage, one can study void properties in the Ag(001) or in the Ag(111) part of the wires.

To study voids in the Ag(111) part of the wires, a positive voltage of 3.7 V was applied to the Ag(001) part of the test structure, resulting in an electrical current of 119 mA and an initial current density of 1.2×10^7 A/cm^2. The electrons propagate from the Ag(111) part to the Ag(001) part of the wires. During electrical stressing an image sequence was captured *in situ* with a LEO 440 SEM with a frame rate of

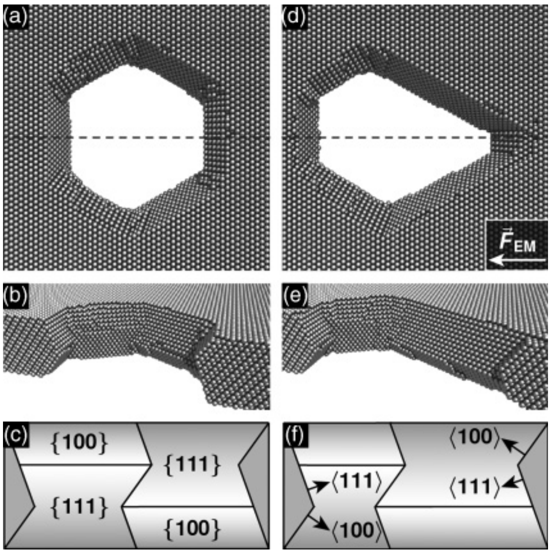

FIG. 4. Void shapes in a (111)-oriented system. (a) Without an electromigration force, the initially round void (see Fig. 3) becomes hexagonal. (b) Upper half of the system in (a) shown from the side. (c) Schematic view of the inner void surface. (d)–(f) Corresponding figures with $\Delta E_{\mathrm{EM}} = 0.005$ eV. This time the void becomes pointed against the $\vec{F}_{\mathrm{EM}}$ direction.

one image per five minutes. Figure 5 shows the test structure after 193 min of electrical stressing. In the image sequence one can observe the voids (dark features) moving to the right and hillocks (bright features) moving to the left. In the image sequence, one can also observe that some voids and hillocks are stationary and others agglomerate to the large voids on the right next to the wires. The voids are predominantly visible in the Ag(111) part of the structure and especially the large voids on the right-hand side have similar shapes as are predicted by the simulations for voids in a (111)-oriented Ag film. Both the experimental and the simulated voids reflect the symmetry of the Ag lattice in the [111] direction with angles of integer multiples of 60°.

B. (001)-oriented Ag film

In contrast to the [111] orientation of the fcc crystal, the [001] orientation has a fourfold symmetry. This is also reflected in the void form in a Ag film with a (001)-top surface. The initially round void shape (see Fig. 3) becomes rectangular after 3×10^8 kMC steps [Fig. 6(a)]. Now, the upper half of the void surface consists of four almost equally sized {111} facets. This is again independent of the exact initial void form.

Figure 6(b) shows the void in Fig. 6(a) from the side after cutting it along the dotted line and Figs. 6(c) and 6(f) show the lateral facets of the void surface in a schematic scheme. A (001) symmetry plane in the middle of the film is revealed. So, the complete void surface now consists of the eight possible {111} facets.

Atoms leaving the void surface gather on the top or bottom surface and build islands, to the extent that complete atom layers of the void surface are removed. As a result the void grows during simulation. The void growth is accompanied by a reduction of the system energy, due to the shrinkage of the energetically less favorable {100} facets.

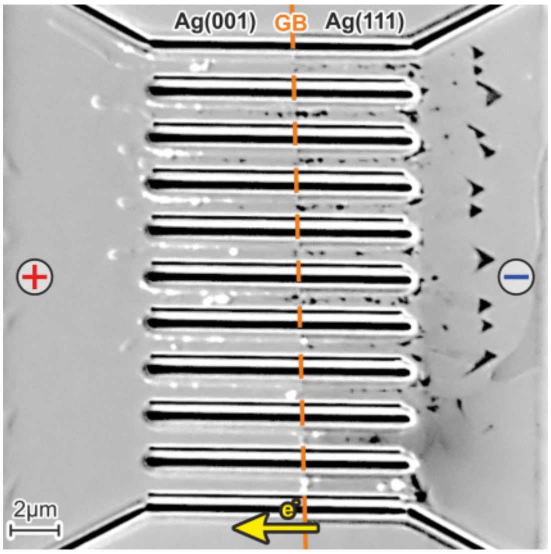

FIG. 5. (Color online) SEM image of an electromigration test structure of ten parallel bicrystalline Ag wires after electrical stressing. On the left side of the grain boundary (indicated by the orange dashed line) the [001] direction of the Ag crystal is normal to the surface. On the right side, the [111] direction of the grain is oriented normal to the surface. For 193 min a current of 119 mA was applied to the wires. The direction of electron motion was from the left to the right [from the Ag(111) part of the wires to the Ag(001) part]. Voids of the characteristic triangular shape, corresponding to the symmetry of the Ag(111) part, are visible on the right-hand side of the image.

This time, applying an electromigration force ($\Delta E_{\mathrm{EM}} = 0.005$ eV) does not lead to a different void shape [Fig. 6(d)]. But after the same amount of kMC steps the void has become larger and hence the film thicker. The electromigration force assists the void growth by driving atoms out of the void in $\vec{F}_{\mathrm{EM}}$ direction. These atoms gather on the upwind void side due to the periodic boundary conditions, where the void edge builds a barrier for the adatoms [Fig. 6(e)]. This results in a drift of the void center due to the asymmetric growth in the $\vec{F}_{\mathrm{EM}}$ direction. The void remains rectangular but the length-to-width ratio changes. It becomes somewhat larger perpendicular to $\vec{F}_{\mathrm{EM}}$.

The growth of the simulated voids in the (001)-oriented film could have happened with the (111)-oriented film, too. But a high adatom density on the top or bottom surface, that leads to the nucleation of an island, was not achieved. The reason is the difference of the activation energy for an adatom hopping over a {100}/{111} edge [Fig. 2(a)] starting either from a $Z = 3$ site on the {111} surface or a $Z = 4$ site on the {100} surface. In the model, the binding energy at the intermediate, unstable site is the same for both processes ($E_{\mathrm{b},Z=2} = -1.971$ eV), but the binding energy at the initial site is lower on the higher coordinated {100} surface ($E_{\mathrm{b}}^{\{100\}} = -2.531$ eV $\Rightarrow \mathrm{E}_{\mathrm{a}}^{\{100\}} = 0.58$ eV; $E_{\mathrm{b}}^{\{111\}} = -2.285$ eV $\Rightarrow \mathrm{E}_{\mathrm{a}}^{\{111\}} = 0.338$ eV. Thus an increase of the adatom density on the (001)-oriented film is favored, because the adatom can hop more easily out of the void than into it. For the (111)-oriented film, the activation energies are either the same [{111}/{111} edge, Fig. 2(b)] or hopping into

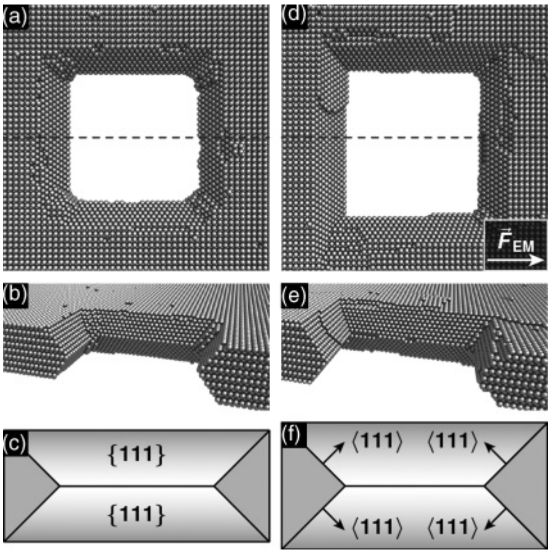

FIG. 6. Void shapes in a (001)-oriented system. (a) Without an electromigration force, the initially round void (see Fig. 3) becomes rectangular. (b) Upper half of the system in (a) shown from the side. (c) Schematic scheme of the inner void surface. (d)–(f) Corresponding figures with $\Delta E_{\mathrm{EM}} = 0.005$ eV.

the void is favored [{100}/{111} edge, Fig. 2(a)]. As a result, the simulated voids in the (001)-oriented film are not stable in contrast to those in a (111)-oriented film.

Figure 7 shows another test structure of ten parallel bicrystalline Ag nanowires structured with FIB similar to the test structure shown in Fig. 5. Here, a negative voltage of 4 V was applied to the Ag(001) part of the wires, resulting in an electrical current of 141 mA and an initial current density of 1.4×10^7 A/cm^2. Again, the grain boundary is marked by an orange dashed line. The Ag(001) part of the wires is left in Fig. 7 and the Ag(111) part is on the right-hand side in Fig. 7. Figure 7 is taken from the *in situ* captured image sequence and shows the test structure after 1189 min.

In Fig. 7 one can predominantly find hillocks (bright features) on the right side of the wires and voids (dark features) on the left-hand side. Here, the voids are propagating to the left. Some voids have agglomerated and have formed the large voids on the left side next to the wires. These voids show similar shapes as were predicted by the simulations for void shapes in a (001)-oriented Ag film. The voids have pronounced 90° angles. But especially the downwind side of the voids, in which the electromigration force points, is not as straight, as one would expect from the simulations.

C. Comparison between experiment and simulation

Both experiment and simulation produce void shapes that reflect the symmetry of the crystal. Moreover, the void shapes are also determined by the electromigration force. For Ag(111) pointed void shapes are observed. The tip exhibits an angle of 60° (Figs. 4 and 5) both in experiment and simulation. The experiment does not tell the direction of $\vec{F}_{\mathrm{EM}}$, however. In the simulation with $\vec{F}_{\mathrm{EM}}$ in the $[\bar{1}\bar{1}2]$ direction, the void tip points in the opposite direction of the electromigration force. In the experiment the void tip points to the negative electrode. The combination of these results indicates that the wind force is the dominating electromigration force in our bicrystalline test structures. This is in line with the observed drift direction of the voids and islands, assuming surface diffusion as the dominating drift mechanism.[18] When the current direction is reversed, voids with their tip in the opposite direction are observed, confirming that the electromigration force determines the void shape.

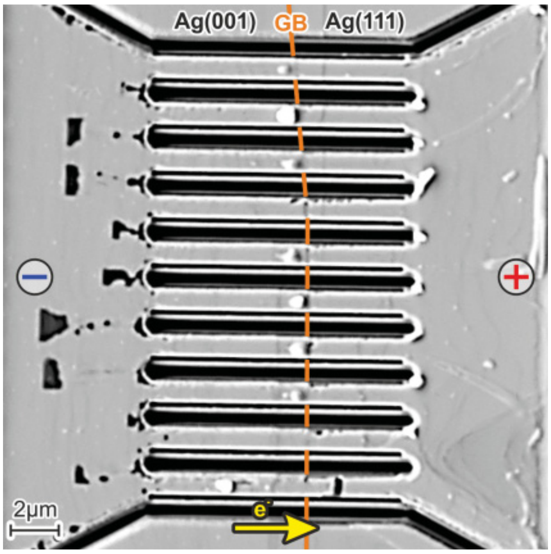

FIG. 7. (Color online) SEM image of an electromigration test structure of ten parallel bicrystalline Ag wires after electrical stressing. On the left side of the grain boundary (indicated by the orange dashed line) the [001] direction of the Ag crystal is normal to the surface. On the right side, the [111] direction of the grain is oriented normal to the surface. For 1189 min a current of 141 mA was applied to the wires. The direction of electron motion was from the Ag(001) part of the wires to the Ag(111) part. Voids of the characteristic rectangular shape, corresponding to the symmetry of the Ag(001) part, are visible on the left side of the image.

For Ag(001), we observe the same drift direction, with respect to the polarity, which also implies that the wind force is the dominating electromigration force. Both simulation and experiment show rectangular void shapes (Figs. 6 and 7). With the current in ⟨110⟩ direction, the voids are oriented with their flat sides perpendicular to the current direction. This is consistent with previous results for two-dimensional voids on a Cu(001) surface made by Mehl *et al.*[19]

The voids in the experiment are one or even two orders of magnitude larger than the ones that could be simulated. Nevertheless they reflect the symmetry of the crystal, as predicted by the lattice simulations. Isotropic continuum simulations,[8] in contrast, showed much more complex void shapes. Based on the equal angles at the upwind void sides, we conclude that the inner facetting of the voids in the experiment is the same as the one in the simulation.

In two dimensions Mehl *et al.*[19] identified the escape of an atom from a fully occupied facet, as the limiting drift process. The detachment of the remaining atoms is, once a vacancy nucleus exists, comparably fast, leading to a row by row void drift. Because in three dimensions the void consists of few large facets, we find in the simulation that the nucleation of a vacancy nucleus on the upwind void facets is the limiting drift mechanism, as in the two-dimensional case.[19]

In the experiment the downwind void sides are comparatively rough, in contrast to what we find in the simulation. A possible explanation for this discrepancy is that the voids in the simulation are one or even two orders of magnitude smaller. Thus it is not very likely that a rough void surface, still consisting of low-energy facets, occurs. To bridge the length scales between experiment and simulation, an atomistic kMC model that enables the simulation of equally sized voids over long enough time scales is desirable for the future.

Moreover, in the simulation the electromigration force is constant. In the experiment the current density differs locally. Because the electrons have to bypass the void, the electromigration force is largest where the cross section of the wire is the smallest. For voids in the Ag(111) film, Figs. 4 and 5, this applies to the top and bottom void corners. Moreover, the electromigration force in the wind shadow of the void at the downwind side should be very small. Thus for Ag(111), atoms from the top and bottom void corners drift to the downwind void edge, where they are no longer exposed to a strong electromigration force.

In the experiment an agglomeration of small, faster drifting voids to larger ones can be observed on the downwind void side. This can lead to asymmetric void shapes, e.g., an elongated void corner (Fig. 5). Such an influence due to the agglomeration of voids is excluded in our simulations, because it would require much bigger systems and simulation times.

We believe that among the discussed three effects the most important one is the inhomogeneity of the electromigration force. Thus the implementation of a locally varying electromigration force, which on an atomistic scale is computationally very demanding, is desirable.

The simulation results presented in this paper are independent of the initial void form. To rule out the influence of the PBCs, we repeated the simulations with OBCs. The same void shapes can be observed. Also in the experiment the boundary conditions, such as the upwind or downwind presence of a grain boundary, do not influence the void shapes. Voids, in both Ag(111) and Ag(001), drifting toward the grain boundary, exhibit the equal void shapes and change to the opposite type of shape, when crossing the grain boundary.

V. CONCLUSIONS

We were able to develop a three-dimensional, atomistic model that is fast enough to investigate electromigration in relatively large systems, at least under accelerated conditions. The computationally very expensive binding-energy calculation for a many-body potential could be avoided by using an empirical many-body correction that includes elastic effects. By utilizing a workaround, we were able to avoid the implementation of hcp sites.

The simulations show a clear dependency between the crystallographic orientation of a monocrystalline Ag film and the electromigration induced void shape. For a (111)-oriented Ag film, a characteristic facetting of the void surface consisting of low index {111} and {100} facet leads, together with the electromigration, to a pointed (60°) void shape. The voids are oriented with their tip in the $(-\vec{F}_{\mathrm{EM}})$ direction. For a (001)-oriented Ag film rectangular void shapes are obtained, consisting of {111} facets.

These results are confirmed by experimental observations for voids in the Ag(111) and Ag(001) part of a bicrystalline Ag nanowire, where the wind force was identified as the dominating electromigration force. The experimentally observed rougher void shapes on the downwind void sides arise, inter alia by the void size difference between experiment and simulation and the locally differing electromigration force. To overcome these limitations we are currently implementing a parallelization of the program and working on a more sophisticated model for the $\vec{F}_{\mathrm{EM}}$ calculation.

ACKNOWLEDGMENTS

Financial support from the Deutsche Forschungsgemeinschaft through SFB616 “Energy Dissipation at Surfaces” is gratefully acknowledged. We thank A. Lorke for the access to the FIB system and R. Zinetullin for helpful discussions.

---

[*] andreas.latz@uni-due.de

[1] J. R. Lloyd, J. Phys. D **32**, R109 (1999).

[2] E. Arzt, O. Kraft, and U. E. Möckl, Phys. Bl. **52**, 227 (1996).

[3] R. S. Sorbello, Solid State Phys. **51**, 159 (1997) .

[4] A. Scorzoni, B. Neri, C. Caprile, and F. Fantini, Mater. Sci. Rep. **7**, 143 (1991).

[5] C. M. Tan and A. Roy, Mater. Sci. Eng. R **58**, 1 (2007).

[6] M. A. Korhonen, P. Borgesen, D. D. Brown, and C.-Y. Li, J. Appl. Phys. **74**, 4995 (1993).

[7] B. D. Knowlton, J. J. Clement, and C. V. Thompson, J. Appl. Phys. **81**, 6073 (1997).

[8] M. Schimschak and J. Krug, Phys. Rev. Lett. **80**, 1674 (1998).

[9] S. A. Chizhik, A. A. Matvienko, A. A. Sidelnikov, and J. Proost, J. Appl. Phys. **88**, 3301 (2000).

[10] P. Kuhn, J. Krug, F. Hausser, and A. Voigt, Phys. Rev. Lett. **94**, 166105 (2005).

[11] R. M. Bradley and K. Wu, Phys. Rev. E **50**, R631 (1994).

[12] C. Pennetta, L. Reggiani, G. Trefán, F. Fantini, A. Scorzoni, and I. Munari, J. Phys. D **34**, 1421 (2001).

[13] C. Pennetta, E. Alfinito, L. Reggiani, F. Fantini, I. DeMunari, and A. Scorzoni, Phys. Rev. B **70**, 174305 (2004).

[14] M. Rusanen, P. Kuhn, and J. Krug, Phys. Rev. B **74**, 245423 (2006).

[15] A. B. Bortz, M. H. Kalos, and J. L. Lebowitz, J. Comput. Phys. **17**, 10 (1975).

[16] A. F. Voter, Phys. Rev. B **34**, 6819 (1986).

[17] A. F. Voter, in *Radiation Effects in Solids*, edited by K. E. Sickafus, E. A. Kotomin, and B. P. Uberuaga (Springer, Dordrecht, 2007), pp. 1–23.

[18] C. Tao, W. G. Cullen, and E. D. Williams, Science **328**, 736 (2010).

[19] H. Mehl, O. Biham, O. Millo, and M. Karimi, Phys. Rev. B **61**, 4975 (2000).

[20] T. V. Zaporozhets, A. M. Gusak, K. N. Tu, and S. G. Mhaisalkar, J. Appl. Phys. **98**, 103508 (2005).

[21] M. S. Daw and M. I. Baskes, Phys. Rev. B **29**, 6443 (1984).

[22] F. Cleri and V. Rosato, Phys. Rev. B **48**, 22 (1993).

[23] R. Zinetullin, Ph.D. thesis, Universität Duisburg-Essen, Duisburg, 2010, [http://duepublico.uni-duisburg-essen.de/servlets/DocumentServlet?id=23584].

[24] D. Wall, S. Thikonov, S. Sindermann, D. Spoddig, C. Hassel, M. Horn-von Hoegen, and F.-J. Meyer zu Heringdorf, IBM J. Res. Dev. **55**, 9 (2011).

[25] S. Sindermann, C. Witt, D. Spoddig, M. Horn-von Hoegen, G. Dumpich, and F.-J. Meyer zu Heringdorf, The Review of Scientific Instruments **82**, 123907 (2011).

[26] T. Ala-Nissila, R. Ferrando, and S. C. Ying, Adv. Phys. **51**, 949 (2002).

[27] J. L. Blue, I. Beichl, and F. Sullivan, Phys. Rev. E **51**, 867 (1995).

[28] A. Chatterjee and D. G. Vlachos, J. Comput.-Aided Mater. Des. **14**, 253 (2007).

[29] Z.-H. Huang and R. E. Allen, J. Vac. Sci. Technol. A **9**, 876 (1991).

[30] See Supplemental Material at http://link.aps.org/supplemental/10.1103/PhysRevB.85.035449 for figures of the 52 utilized neighbor configurations, and a table with the corresponding many-body corrections, as well as a table with ΔE for 17 key elementary processes.

[31] J. R. Black, IEEE Trans. Electron Dev. **16**, 338 (1969).

[32] B. Stahlmecke, F.-J. Meyer zu Heringdorf, L. I. Chelaru, M. Horn-von Hoegen, G. Dumpich, and K. R. Roos, Appl. Phys. Lett. **88**, 053122 (2006).

[33] K.-N. Tu, in *Solder Joint Technology*, Vol. 117 of Springer Series in Materials Science (Springer, New York, 2007), pp. 211–243, [http://dx.doi.org/10.1007/978-0-387-38892-2_8].

[34] J. P. Dekker and A. Lodder, J. Appl. Phys. **84**, 1958 (1998).

[35] D. R. Lide, *CRC Handbook of Chemistry and Physics,* 84th ed. (CRC Press, Boca Raton, 2004).

[36] M. R. Castell, Phys. Rev. B **68**, 235411 (2003).

[37] Y. Wen and J. Zhang, Solid State Commun. **144**, 163 (2007).

[38] Y. Fujikawa, T. Sakurai, and R. M. Tromp, Phys. Rev. Lett. **100**, 126803 (2008).

[39] Y. Fujikawa, T. Sakurai, and R. M. Tromp, Phys. Rev. B **79**, 121401 (2009).